Dynamical image potential and induced forces for charged particles moving parallel to a solid surface

Néstor R. Arista
División Colisiones Atómicas, Centro Atómico Bariloche and Instituto Balseiro, Comisión Nacional de Energía Atómica, RA-8400 Bariloche, Argentina
(Received 27 July 1993)

The dynamical image potential and ensuing forces induced by a charged particle moving parallel to a solid surface are investigated by using a dielectric formulation for semi-infinite dispersive media. The adiabatic behavior of the field in the asymptotic range is discussed in a general way using a multipole expansion. Several calculations illustrate the behavior of the field using both a simple model, where the surface response is approximated by a single plasma resonance, and a more realistic representation of the medium based upon the empirical information on the optical constants for various solids (Al, Cu, Ag, and Au). The model parameters may be adjusted to provide very good agreement with the optical-data integrations of the stopping and lateral forces on the moving charge. On the other hand, important differences in the description of the wake potential using either the simple plasma resonance model, or the optical-data representation, are obtained for Cu, Ag, and Au.

PACS number(s): 34.50.Bw, 79.20.Rf, 78.90.+t

I. INTRODUCTION

Different aspects of the interaction between fast moving particles and solid surfaces have been investigated theoretically and experimentally in recent literature, as well as applications to relevant processes of electronic and atomic interactions with surfaces.

The theoretical basis for these studies was developed in the 1970s, based on earlier studies of surface-plasmon excitations by Ritchie [1,2]. One of the important developments in this area was the extension of the dielectric formalism to treat the interaction of external charges with a semi-infinite medium [2–5] or the alternative Hamiltonian approach [6,7] where the surface excitations are described in terms of quantized modes. The latter approach is usually applicable to ideal metal surfaces, while the former approach permits, in principle, the introduction of more realistic response functions for dispersive media [8], although so far most of the calculations have been made using free-electron-gas models.

One of the points of interest in these studies is the calculation of the induced field or *dynamical image potential* produced by a charged particle moving close to the surface. Investigations of this problem have been made by a number of authors [3–5, 9–11] using the dielectric formalism for semi-infinite media, and the electron gas random-phase approximation (RPA) dielectric function. A detailed description of the surface *wake* potential according to the RPA model has been given recently by García de Abajo and Echenique [11], who also reviewed previous work in this area.

On the other hand, important experimental developments have been made in the last few years, which open new ways to study atomic processes at solid surfaces and the role of dynamical effects in particle-surface interactions. In particular, we mention the following.

(i) Energy losses of ions specularly reflected from solid surfaces [12–15].

(ii) The dissociation of molecular ions in glancing incidence experiments [16].

(iii) The skipping motion of ions at surfaces [17,18]

(iv) Image-potential effects on fast-proton trajectories in surface scattering [19].

(v) Shifts in the atomic energy levels of ions moving close to a solid surface [20].

(vi) Convoy electrons emission from solid surfaces in beam-foil (transmission) [21,22] and in grazing-incidence (reflection) experiments [23–25].

(vii) Acceleration effects on convoy electrons produced in grazing-angle scattering of ions at surfaces [26–31].

In some of these cases the electronic structure of the medium has rather complicated features which cannot be fully represented by a free-electron-gas model, and hence a study of the problem from an alternative approach may be useful.

The purpose of this work is to investigate the properties of the dynamical field induced by particles moving in a parallel trajectory and close to a vacuum-solid interface. We will use here both a simplified dielectric description in the form of a single surface-plasma resonance, and a more realistic representation of the response function for various solids of experimental interest (Al, Cu, Ag, and Au) by incorporating optical data for each element. We will use tabulated results for the dielectric function taken from experiments and optical-data analyses over a very wide range of frequencies, from the infrared to the x-ray region [32].

In Sec. II the basic dielectric formulation is reviewed and some useful results for a simple plasma-resonance model are derived. This section contains some results already derived by previous authors which are included here to illustrate and compare with our results. A general multipole expansion of the field is considered in Sec. III, and is exemplified for the previous case of a simple plasma-resonance model. In Sec. IV the information on the optical constants for various elements is used to cal-

culate the induced potential and the values of the stopping and lateral forces. These values will be compared with the ones obtained from the plasma-resonance model with properly chosen parameters for each element. Possible applications of these results to processes of current interest will be briefly considered in Sec. V, which also includes a final discussion and conclusions.

II. SIMPLE MODEL DERIVATIONS

A. Calculation of the induced potential

Let us consider a particle of charge Q moving parallel to a plane solid surface (located at $z=0$) with uniform velocity $\mathbf{v}$ along the x direction as indicated in Fig. 1. The response of the medium will be characterized by a frequency-dependent dielectric function $\epsilon(\omega)$. The constant distance between the particle and the surface will be denoted by z_0. We will consider the origin of coordinates 0 to be located on the surface and moving with the ion velocity $\mathbf{v}$, cf. Fig. 1. Thus, the particle position is given by $\mathbf{r}_0=(0,0,z_0)$.

As can be shown from simple translational invariance arguments, the induced electric potential $\phi_{\text{ind}}(\mathbf{r})$ in this frame of reference is independent of time, and, according to the dielectric formalism [4,5], its value may be written as

$$\phi_{\text{ind}}(\mathbf{r})=\frac{4\pi Q}{(2\pi)^3}\int d^2\kappa\int_{-\infty}^{\infty}dq\frac{e^{i\boldsymbol{\kappa}\cdot\boldsymbol{\rho}}e^{iqz}}{(\kappa^2+q^2)}\left[\exp(iqz_0)-\exp(-\kappa z_0)\left[\frac{2\epsilon(\omega)}{\epsilon(\omega)+1}\right]\right]_{\omega=\boldsymbol{\kappa}\cdot\mathbf{v}}. \tag{1}$$

After some mathematical transformations, this integral can be conveniently expressed in the x-z plane as follows (see the Appendix):

$$\phi_{\text{ind}}(x,z)=\frac{-Q}{\pi v}\int_0^{\infty}\frac{d\xi}{(1+\xi^2)^{1/2}}\int_{-\infty}^{\infty}d\omega\left[\frac{\epsilon(\omega)-1}{\epsilon(\omega)+1}\right]e^{i\omega x/v}\cos\left[\xi\frac{\omega}{v}(z+z_0)\right]. \tag{2}$$

Let us consider now the evaluation of this integral for a simple model consisting of a single plasma resonance to describe the surface response. In this model the surface-plasma poles are shifted to complex frequencies: $\pm\omega_s'-i\gamma/2$, where $\omega_s=\omega_p/\sqrt{2}$ is the surface-plasmon frequency, $\omega_P=(4\pi ne^2/m)^{1/2}$ is the bulk-plasmon frequency, γ is the damping rate, and $\omega_s'=(\omega_s^2-\gamma^2/4)^{1/2}$ is the shifted surface-plasmon frequency. Therefore, the surface-response function $[\epsilon(\omega)-1]/[\epsilon(\omega)+1]$ in Eq. (2) can be written as follows:

$$\frac{\epsilon(\omega)-1}{\epsilon(\omega)+1}=\frac{\omega_s^2}{2\omega_s'}\left[\frac{1}{\omega+\omega_s'+i\gamma/2}-\frac{1}{\omega-\omega_s'+i\gamma/2}\right]. \tag{3}$$

Using this form, Eq. (2) can be integrated in the complex ω plane, and we obtain

$$\phi_{\text{ind}}(x,z)=-\frac{Q}{v}\frac{\omega_s^2}{\omega_s'}\times\int_{\xi_0(x,z)}^{\infty}d\xi\frac{\sin[\omega_s'\tau(x,z,\xi)]}{(1+\xi^2)^{1/2}}\times\exp\left[-\frac{\gamma}{2}\tau(x,z,\xi)\right], \tag{4}$$

where

$$\xi_0(x,z)=\frac{x}{(z+z_0)}, \tag{5a}$$

$$\tau(x,z,\xi)=[\xi(z+z_0)-x]/v. \tag{5b}$$

Equation (4) provides a useful integral representation of the surface wake potential. In Fig. 2 we illustrate the shape of the potential calculated from this expression. Figure 2(a) shows the induced potential $\phi_{\text{ind}}(x,z_0)$, and the electric-field components $E_x(x,z_0)$, $E_z(x,z_0)$, for points x along the particle trajectory for a particle with velocity $v=10$ a.u. (atomic units) at a distance $z_0=5$ a.u. from the surface. It has the shape of a *wake potential* with wavelength $\lambda=2\pi v/\omega_s$, and with the electric-field components E_z and E_x oscillating in and out of phase with ϕ_{ind}.

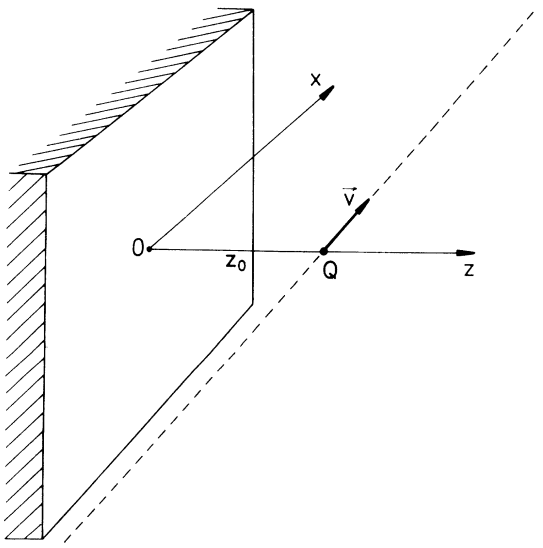

FIG. 1. A particle with charge Q and velocity v, moving along the x direction at a distance z_0 from a plane surface located at $z=0$. The origin of coordinates is taken at the point 0, which moves along the surface isotachycally with the particle.

Figure 2(b) illustrates the variation of the wake potential and electric field at a constant value of $x=-20$ a.u. (behind the particle) and as a function of z (i.e., this shows a *cut* of the wake potential along a direction perpendicular to the surface and to the particle trajectory). The maximum amplitude of the wake field occurs at the surface, as can be expected for surface-plasmon fields [1,6]. (One could notice a basic difference with the wake field in the bulk, i.e., when the particle moves inside the material where, as is rather well known, the maximum amplitude occurs for points along the particle trajectory [33]).

From Eq. (4) we can obtain the value of the induced potential at the charge (for simplicity, here we use $\phi^0_{\rm ind}$ to denote values taken at the charge position), namely

$$\phi^0_{\rm ind}\equiv\phi_{\rm ind}(0,z_0)=-\frac{Q}{v}\frac{\omega_s^2}{\omega_s'}\int_0^\infty d\xi\frac{\sin(\alpha\xi)}{(1+\xi^2)^{1/2}}e^{-\beta\xi} \tag{6}$$

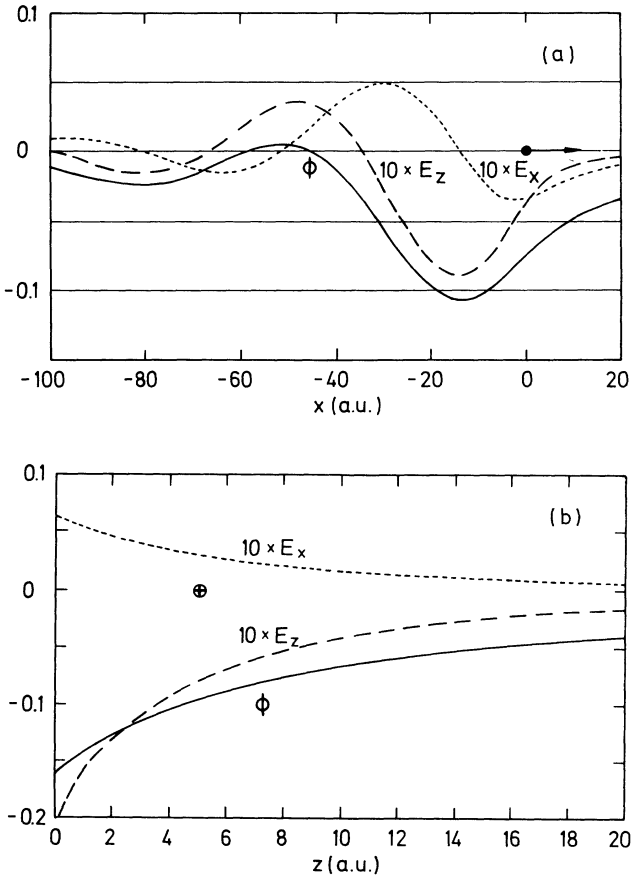

FIG. 2. Induced wake potential $\phi_{\rm ind}(x,z)$ and electric-field components $E_x(x,z)$, $E_z(x,z)$, for a particle moving with velocity $v=10$ a.u. at a distance $z_0=5$ a.u. from the surface. The surface response is characterized here by the parameters $\omega_s=1$ a.u. and $\gamma=0.5$ a.u. (a) Longitudinal view of the field, for $z=z_0$ and as a function of x (i.e., along the particle trajectory); the solid circle shows the instantaneous position of the charge, which is moving to the right. (b) Transverse view of the field along the z direction (perpendicular to the solid surface), taken at a constant value of $x=-20$ a.u.; the crossed circle here indicates the point of intersection of the particle trajectory (perpendicular to the figure plane).

with $\alpha=2\omega_s' z_0/v$ and $\beta=\gamma z_0/v$.

It is of interest to quote here the following limiting values.

(i) $v\to 0$.

Approximating $(1+\xi^2)^{-1/2}\cong 1-\xi^2/2$ in Eq. (6) we obtain

$$\phi^0_{\rm ind}\cong-\frac{Q}{2z_0}-\frac{Q}{(2z_0)^3}\left[\frac{v}{\omega_s}\right]^2\left[1-\frac{\gamma^2}{\omega_s^2}\right]. \tag{7}$$

(ii) $v\to\infty$, $\gamma\to 0$.

For $\gamma\to 0$, the integral in Eq. (6) becomes

$$\int_0^\infty\frac{d\xi}{(1+\xi^2)^{1/2}}\sin(\alpha\xi)=\frac{\pi}{2}[I_0(\alpha)-L_0(\alpha)], \tag{8}$$

where I_0 and L_0 denote a Bessel function (of imaginary argument) and a modified Struve function, respectively [34]. Taking the limit $v\to\infty$ (i.e., $\alpha\to 0$) in $I_0(\alpha)$ and $L_0(\alpha)$ [34] we get

$$\phi^0_{\rm ind}\cong-\frac{Q\omega_s}{v}\left[\frac{\pi}{2}-\frac{2\omega_s z_0}{v}\right]. \tag{9}$$

The first term here gives the value of $\phi^0_{\rm ind}$ for $z_0\ll v/\omega_s$, which is independent of z_0 (contact limit).

B. Force components

From Eq. (4) we can calculate the induced electric field $\mathbf{E}_{\rm ind}=-\nabla\phi_{\rm ind}$, and then we separate the x and z components to obtain expressions for the stopping and lateral forces acting on the particle. This yields the following.

(i) Stopping force

$$F_x=-\frac{Q^2\omega_s^2}{v^2}\int_0^\infty\frac{d\xi}{(1+\xi^2)^{1/2}}\left[\cos(\alpha\xi)-\left[\frac{\gamma}{2\omega_s'}\right]\sin(\alpha\xi)\right]e^{-\beta\xi}, \tag{10}$$

(ii) Lateral force

$$F_z=\frac{Q^2\omega_s^2}{v^2}\int_0^\infty\frac{\xi d\xi}{(1+\xi^2)^{1/2}}\left[\cos(\alpha\xi)-\left[\frac{\gamma}{2\omega_s'}\right]\sin(\alpha\xi)\right]e^{-\beta\xi}, \tag{11}$$

where $\alpha=2\omega_s' z_0/v$ and $\beta=\gamma z_0/v$.

By definition, the stopping force is opposite to the particle velocity $\mathbf{v}$ ($-x$ direction), while the lateral force is perpendicular to the particle trajectory and to the interface ($-z$ direction). It can be shown from Eq. (11) that for $v\to 0$, F_z reduces to the static image force: $F_z\cong-Q^2/4z_0^2$.

Illustrative values of these forces for various metals will be given in Sec. IV, but we shall quote here the following limits of interest for the stopping force.

(i) $\gamma \to 0$.

In this limit the integral in Eq. (10) reduces to a Bessel function,

$$\int_0^\infty \frac{d\xi}{(1+\xi^2)^{1/2}} \cos(\alpha\xi) = K_0(\alpha) , \tag{12}$$

and we obtain a well-known approximation to the stopping force corresponding to a sharp plasma resonance [35], namely

$$F_x = -\left[\frac{Q\omega_s}{v}\right]^2 K_0\left[\frac{2\omega_s z_0}{v}\right] . \tag{13}$$

(ii) $v \to 0$.

Here we can use again the expansion $(1+\xi^2)^{-1/2} \cong 1-\xi^2/2$ and performing the integration in Eq. (10) we obtain

$$F_x = -\frac{Q^2}{\omega_s^2}\frac{\gamma v}{(2z_0)^3} . \tag{14}$$

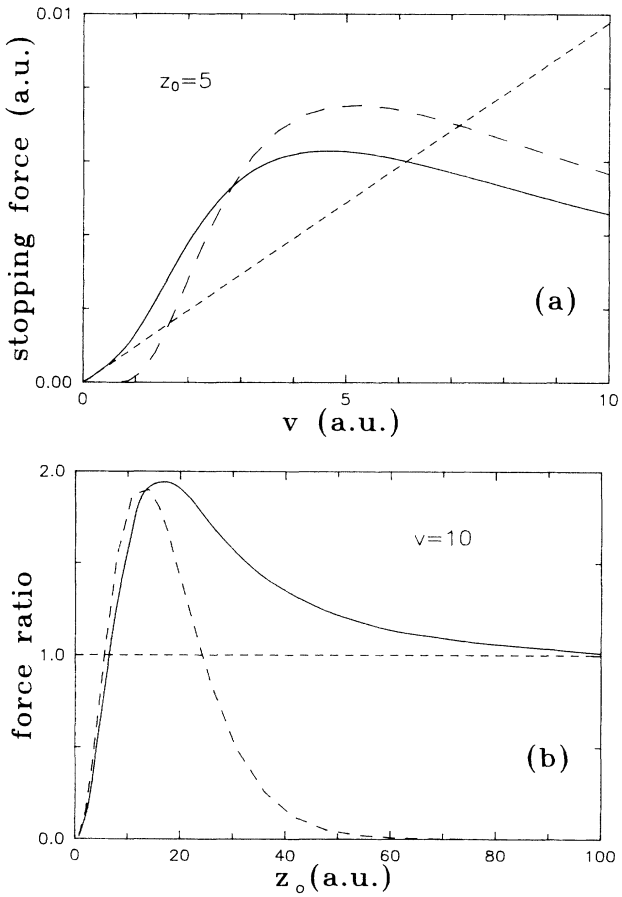

FIG. 3. Comparisons between the stopping force values from Eq. (10) (solid lines) and the approximations of Eq. (13) (dashed lines) corresponding to a sharp resonance, and of Eq. (14) (dotted lines) corresponding to the low-velocity dipole limit. (a) and (b) illustrate the dependence on particle velocity v and distance to the surface z_0. In (b) we show the ratio between the stopping forces evaluated from Eqs. (10) and (13) and the dipole limit of Eq. (14). Notice that the exact force approaches the dipole limit either for low velocities (a) or very large distances (b).

This result is characteristic of the quasiadiabatic regime, and has been derived by various authors [3,9,10]. As will be shown next, this result corresponds to the dipole term in a multipole expansion of the induced field.

The results for the stopping force are illustrated in Fig. 3(a), where we compare the values obtained from the integral in Eq. (10) (solid line), with the approximations from Eqs. (13) (dashed line) and (14) (dotted line), for the case $\omega_s = 1$, $\gamma = 0.5$. The K_0 limit of Eq. (13) does not provide a satisfactory approximation for a rather wide plasma resonance.

From the derivation given above [Eqs. (10) and (11)], it can be seen that the parameter $\alpha \cong 2\omega_s z_0/v$ may be used to characterize the dynamical effects of the interaction, and it gives a criterion to distinguish between the ranges of high or low velocities v, or small or large distances z_0. Physically, the meaning of this parameter can be discussed using the adiabatic Bohr criterion for energy transfer to a harmonic oscillator of frequency ω_s (with an adiabatic distance $\lambda_{ad} = v/\omega_s$). Hence, one should also expect to obtain the quasiadiabatic limit of Eq. (14) in the asymptotic case, when the distance z_0 between the particle trajectory and the surface is much larger than λ_{ad}.

This asymptotic limit is illustrated in Fig. 3(b), which shows the ratio between the force values obtained from Eqs. (10) and (13) and the limit of Eq. (14), as a function of z_0 and for a fixed velocity $v = 10$ a.u. The K_0 approximation decay exponentially for large z_0, while the correct result for large z_0 approaches the dipole limit of Eq. (14).

Thus, Figs. 3(a) and 3(b) illustrate how the exact force approaches the dipole limit either for low velocities, 3(a), or very large distances, 3(b).

III. MULTIPOLE EXPANSION

The multipole expansion of the induced field provides a convenient framework to understand some of the limits already obtained. The standard way to carry out this expansion would be to calculate the induced charge density on the surface (or some equivalent image charge distribution inside the solid) and evaluate the multipole moments of the charge distribution.

On the other hand, one can obtain an expansion of the induced potential in powers of the particle velocity by considering the low-frequency expansion of the integrand in Eq. (1). This approach has been used in particular to approximate the value of the lateral force on an electron beam [36]. It can be shown that the result of these two approaches are identical.

To derive a multipole expansion we first write Eq. (1) (after integrating over q) in the form

$$\phi_{\rm ind}(\mathbf{r}) = \frac{-Q}{2\pi}\int \frac{d^2\kappa}{\kappa} e^{i\boldsymbol{\kappa}\cdot\boldsymbol{\rho}} e^{-\kappa(z+z_0)} F(\omega)\Big|_{\omega=\boldsymbol{\kappa}\cdot\mathbf{v}} \tag{15}$$

where

$$F(\omega) = \frac{\epsilon(\omega)-1}{\epsilon(\omega)+1} . \tag{16}$$

Denoting by κ_1 the x component of $\boldsymbol{\kappa}$, so that $\omega = \kappa_1 v$ in

Eq. (15), we write the Taylor expansion of $F(\omega)$ as follows:

$$F(\omega)=F(0)+(\kappa_1 v)F'(0)+\tfrac{1}{2}(\kappa_1 v)^2F''(0)+\cdots . \quad (17)$$

Using this in Eq. (15) and performing the integrations we get the following expression:

$$\phi_{\rm ind}=-Q\left[\frac{\epsilon(0)-1}{\epsilon(0)+1}\right]\left[\frac{1}{R'}\right]-p_1\frac{\partial}{\partial x}\left[\frac{1}{R'}\right]+q_{11}\frac{\partial^2}{\partial x^2}\left[\frac{1}{R'}\right]+\cdots , \quad (18)$$

where $R'=|\mathbf{r}-\mathbf{r}'_0|=[\rho^2+(z+z_0)^2]^{1/2}$ is the distance between a test point $\mathbf{r}=(\boldsymbol{\rho},z)$ in the vacuum region and the classical image point $\mathbf{r}'_0=(0,-z_0)$ inside the medium.

The first term in Eq. (18) corresponds to the monopole field produced by a fictitious image charge of value

$$Q_{\rm image}=-Q\left[\frac{\epsilon(\omega)-1}{\epsilon(\omega)+1}\right]\Bigg|_{\omega=0} \quad (19)$$

located at the image point $\mathbf{r}'_0$.

The second term in Eq. (18) yields the field of a dipole p_1 oriented parallel to $\hat{\mathbf{x}}$, and moving in the $\hat{\mathbf{x}}$ direction with the same velocity $\mathbf{v}$ as the source charge. The value of the dipole moment, as deduced from Eq. (15), becomes

$$p_1=-iQv\frac{\partial}{\partial\omega}\left[\frac{\epsilon(\omega)-1}{\epsilon(\omega)+1}\right]\Bigg|_{\omega=0} \quad (20)$$

[notice that p_1 is a real quantity, as can be shown from the general property $\epsilon(-\omega)=\epsilon^*(\omega)$].

The third term in Eq. (18) corresponds to the field produced by a quadrupole moment

$$q_{11}=\tfrac{1}{2}Qv^2\frac{\partial^2}{\partial\omega^2}\left[\frac{\epsilon(\omega)-1}{\epsilon(\omega)+1}\right]\Bigg|_{\omega=0} \quad (21)$$

and in a similar way the higher-order moments of the expansion are related to the same-order derivatives of the response function $[(\epsilon-1)/(\epsilon+1)]$. This procedure generates an expansion in powers of the velocity v, which can also be considered an *adiabatic* representation of the dynamical effects, so that with increasing velocities the contribution from higher-order multipole moments grows in a continuous way.

In particular, for the plasma resonance model used before, the values of the first three moments become

$$Q_{\rm image}=-Q , \quad (22a)$$

$$p_1=Q\frac{\gamma v}{\omega_s^2} , \quad (22b)$$

$$q_{11}=Q\frac{v^2}{\omega_s^2} . \quad (22c)$$

Looking back now to the limit of Eq. (14) for the stopping force we can see that it is exactly the field of a dipole of value p_1 located at the image point $\mathbf{r}'_0=(0,-z_0)$, oriented parallel and moving with the same velocity $\mathbf{v}$ as the particle. In this situation, the direction of the dipole electric field at the instantaneous position of the moving particle is always pointing opposite to the particle velocity, and its value gives exactly the stopping force of Eq. (14).

We can additionally note that if the same calculation is performed for the case of an incident particle with a trajectory *perpendicular* to the surface, one obtains an induced dipole moment of exactly the same value as in Eqs. (20) or (22), but oriented now perpendicular to the surface and pointing against the particle velocity $\mathbf{v}$, so that the resulting dipole field will again give rise to a stopping force on the particle. However, the value of the stopping force in this latter case becomes *twice* as large as that for the case of parallel motion. This difference between the stopping forces in the parallel and perpendicular cases has already been noted by previous authors [3,10]. We can give a simple explanation of this factor of 2 using the well-known expression for the dipole electric field

$$\mathbf{E}(r,\theta)=\frac{p}{r^3}(2\cos\theta\hat{\mathbf{r}}+\sin\theta\hat{\boldsymbol{\theta}}) \quad (23)$$

which shows that, for a given r value, the dipole field becomes twice as intense for points close to its axis ($\theta=0$) as perpendicular to it ($\theta=\pi$).

In summary, the difference between the two cases can be explained as a consequence of the dipolar character of the quasiadiabatic approximation. Thus, it turns out to be a rather general relation, not depending on the particular plasma-response function.

IV. DESCRIPTION BASED ON OPTICAL-CONSTANT VALUES

The plasma-resonance model used in the previous sections gives in many cases only a very crude representation of the dielectric properties of real solids. Therefore, it becomes of considerable interest to investigate the values of the dynamical potential and induced forces using more realistic representations of the dielectric function of various elements.

For this purpose, we will now introduce into the formalism the experimental information on the dielectric function for various solids (Al, Cu, Ag, and Au) using the results of optical-data analysis derived from experimental determinations [32]. These experiments cover a very wide range of frequencies, corresponding to photon energies $E=\hbar\omega$ from 10^{-3} to 10^6 eV.

As an example, we show in Figs. 4(a) and 4(b) the real and imaginary parts of the surface response function $[\epsilon(\omega)-1]/[\epsilon(\omega)+1]$ versus the energy $E=\hbar\omega$, for the case of Cu; Figs. 5(a) and 5(b) show the same for the case of Ag. These values were deduced from the empirical values of the real $[\epsilon_1(\omega)]$ and imaginary $[\epsilon_2(\omega)]$ parts of the dielectric function given in Ref. [32]. The dashed curves in Figs. 4 and 5 show rather rough representations of the data using a broad plasma resonance with appropriate parameters, Eq. (3), as will be discussed below. We note here a special feature in the data for Ag (Fig. 5): the peak at $\hbar\omega=3.78$ eV, which corresponds to a very sharp plasma resonance [37].

In order to use these experimental values of the surface

response function $\{[\epsilon(\omega)-1]/[\epsilon(\omega)+1]\}$, it is convenient to integrate first over the variable ξ in Eq. (2). This yields the following expressions for the induced potential and forces acting on the particle.

(i) Induced (wake) potential

$$\phi_{\rm ind}(x,z)=-\frac{2Q}{\pi v}\int_0^\infty d\omega K_0\left[\frac{\omega}{v}(z+z_0)\right]\times\left[\mathrm{Re}\left[\frac{\epsilon(\omega)-1}{\epsilon(\omega)+1}\right]\cos\left[\frac{\omega x}{v}\right]-\mathrm{Im}\left[\frac{\epsilon(\omega)-1}{\epsilon(\omega)+1}\right]\sin\left[\frac{\omega x}{v}\right]\right]. \tag{24}$$

(ii) Stopping force

$$F_x\equiv QE_x=-\frac{2Q^2}{\pi v^2}\int_0^\infty \omega\, d\omega K_0\left[\frac{2\omega z_0}{v}\right]\mathrm{Im}\left[\frac{\epsilon(\omega)-1}{\epsilon(\omega)+1}\right]. \tag{25}$$

(iii) Lateral force

$$F_z\equiv QE_z=-\frac{2Q^2}{\pi v^2}\int_0^\infty \omega\, d\omega K_1\left[\frac{2\omega z_0}{v}\right]\times\mathrm{Re}\left[\frac{\epsilon(\omega)-1}{\epsilon(\omega)+1}\right]. \tag{26}$$

These expressions have been evaluated numerically using the empirical data on the dielectric function in the range from 10^{-3} to 10^6 eV from Ref. [32].

Let us consider first the calculation of the stopping force, Eq. (25). We show in Fig. 6 the values of the stopping forces for Al (a), Cu (b), Ag (c), and Au (d). The solid lines are the results of numerical calculations using the tabulated values of the optical constants for each of these elements [32]. The values calculated in this paper are in all cases for a unit charge $Q=1$.

Now we can consider the question of to what extent a simple plasma resonance, as in the cases shown in Figs. 4 and 5 (dashed lines), could be used to approximate the more realistic results for the stopping forces evaluated here. To test this possibility we found the most appropriate values for the model parameters ω_s and γ, as given in Table I, which are the ones that provide a best overall

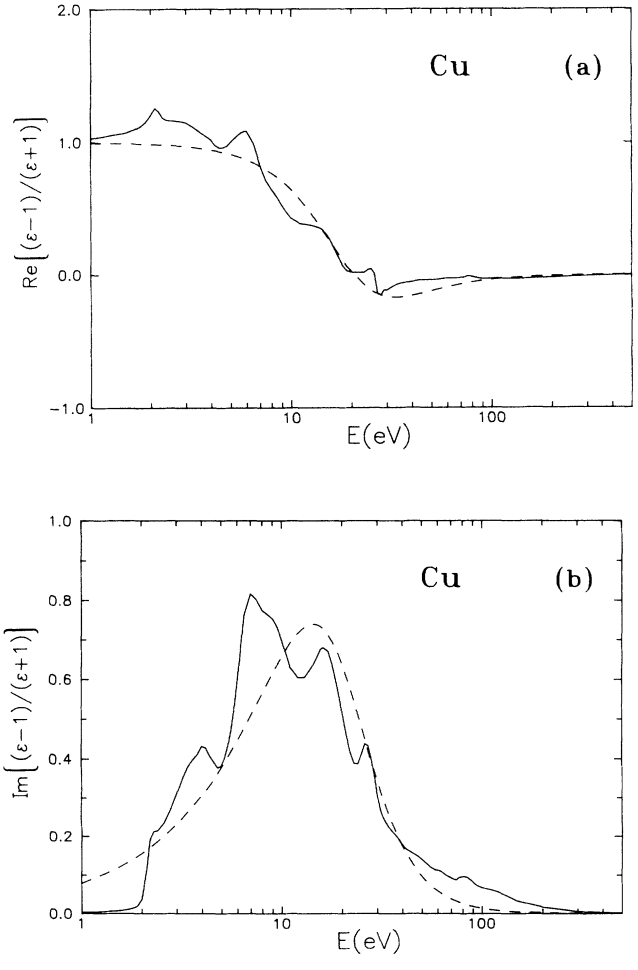

FIG. 4. Values of the surface response function $[\epsilon(\omega)-1]/[\epsilon(\omega)+1]$, versus energy $E=\hbar\omega$, deduced from the experimental data on the optical constants of Cu given in Ref. [32]. The values of the real and imaginary parts are shown in (a) and (b).

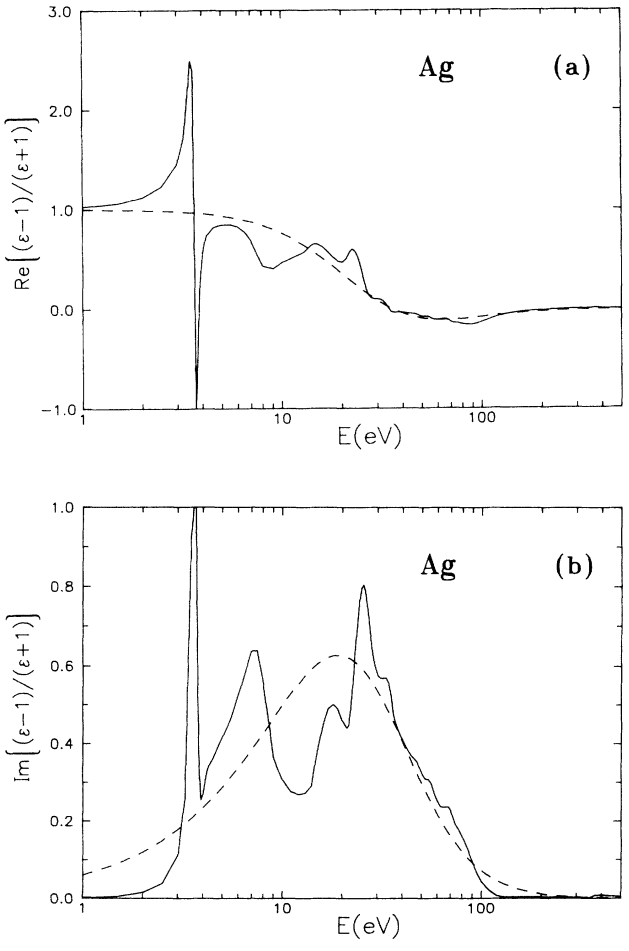

FIG. 5. Same as in Fig. 4, for the case of Ag.

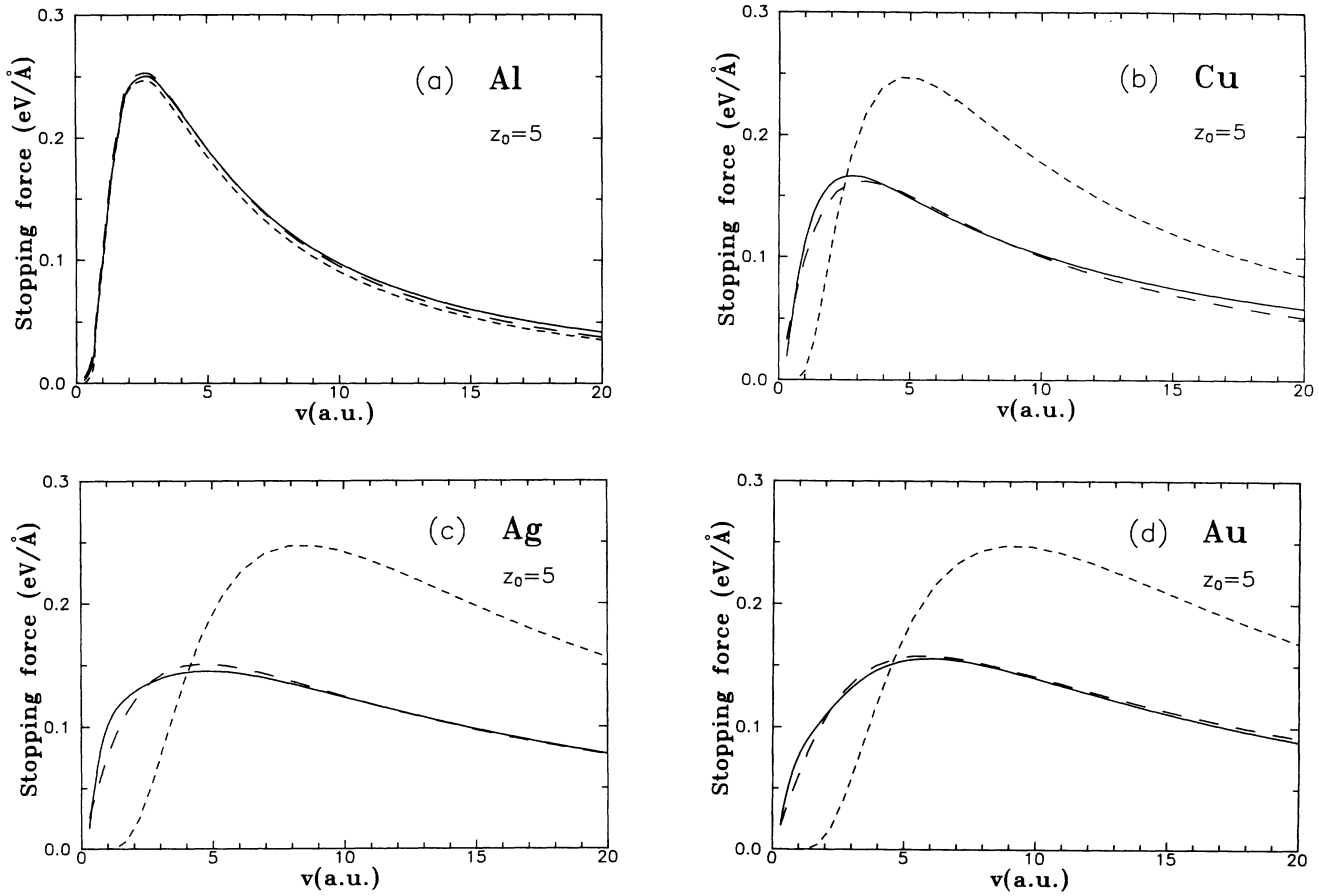

FIG. 6. Comparison between the stopping-force values for (a) Al, (b) Cu, (c) Ag, and (d) Au, according to different calculations. Solid lines: values obtained from Eq. (25) by numerical integrations using the empirical optical-constant values from Ref. [32]; long-dashed lines: calculations using the plasma-resonance model, Eq. (10), with the ω_s and γ values given in Table I; short-dashed lines: analytical approximation of Eq. (13) for a sharp plasma resonance.

representation of the stopping forces, for a rather wide range of distances ($1 < z_0 < 50$ a.u.) and velocities ($1 < v < 20$ a.u.) considered in our calculations.

The long-dashed lines in Figs. 6(a) to 6(d) show the calculations using the plasma-resonance model of Sec. II, Eq. (10), with the values of ω_s and γ given in Table I, while the short-dashed lines show the analytical approximation for a sharp plasma resonance ($\gamma = 0$) given by Eq. (13). These comparisons can be extended to a range of distances z_0 with similar results; for instance, Fig. 7 shows further values of the stopping forces at distances $z_0 = 2$, 5, 10, and 20 a.u. in the case of Ag.

Thus, the values calculated with a plasma-resonance model are in all cases in good agreement with the calculations using the full set of optical data, provided that the parameters of the plasma resonance are adjusted for each element. On the other hand, the results for an ideal free-electron gas, Eq. (13), apply only to materials with a very

TABLE I. Values of the model parameters: characteristic frequency ω_s and width γ, in a.u., for the solids studied in this paper.

Element	ω_s	γ
Al	0.40	0.037
Cu	0.75	1.2
Ag	1.30	2.8
Au	1.41	2.5

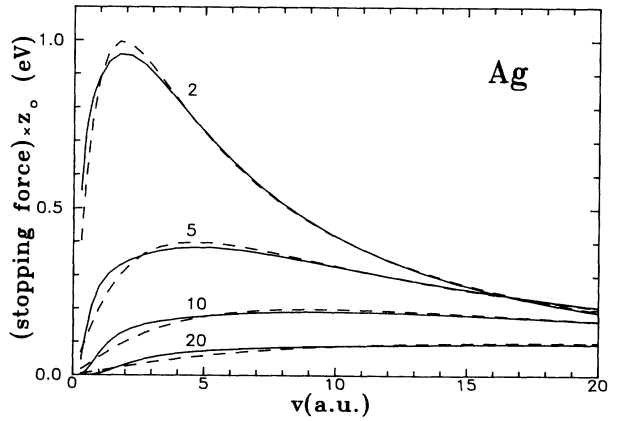

FIG. 7. Stopping force values (multiplied by distance z_0) vs particle velocity v for distances $z_0 = 2$, 5, 10, and 20 a.u. from an Ag surface. Solid lines: values obtained from the integration of the optical data of Ag; dashed lines: calculations using the plasma-resonance model with the ω_s and γ values given in Table I.

narrow plasma resonance, as for Al, but may give erroneous results in other cases.

Using the same ω_s and γ values, we also calculated the lateral forces for each of these metals from Eq. (11), and compared the results with the numerical evaluations from Eq. (26) using the optical data. Figures 8(a) and 8(b) show the comparisons for Ag and Au between the integrations of the optical values (solid lines) and the results from the fitted plasma-resonance model (dashed lines). For comparison, the corresponding values of the stopping forces are also included in the figure. In all the cases considered with this approach we found that the results were in very good agreement.

Finally, in Figs. 9(a) and 9(b), we compare the values of the parallel, 9(a), and perpendicular, 9(b), forces for ions moving close to Al, Cu, Ag, and Au surfaces. We also notice from Figs. 8 and 9 the distinct behavior of the stopping and lateral forces at low velocities. The stopping force is related to the dynamical response of the medium, and therefore it drops to zero for a static charge. In contrast, the lateral force has a finite limit given by the static image potential. Mathematically, this difference arises from Eqs. (25) and (26) where the two forces are determined by the imaginary and real parts of the response function (i.e., the dissipative and conservative parts).

Let us consider now the calculation of the induced potential. First we compare the results for the potential evaluated at the instantaneous position of the moving charge, $\phi^0_{\rm ind}=\phi_{\rm ind}(\mathbf{r}_0)$. This is done in Fig. 10 for fixed distances $z_0=2$, 5, 10, and 20 a.u., as a function of the velocity v, 10(a), and for fixed velocities $v=1$, 2, 5, and 10 a.u., as a function of the distance z_0 10(b). Again, a remarkable agreement is obtained between the empirical optical-data results from Eq. (24), and the resonance model, in the simple form of Eq. (6).

Finally, we consider the evaluation of the wake potential as a function of the distance to the moving charge. In Figs. 11 and 12 we show the values of the induced potential at the surface ($z=0$) as a function of x, where the value $x=0$ corresponds to the instantaneous position of the charge, represented in these figures with a small circle and assumed to be moving to the right (cf. Fig. 1). To illustrate the differences we show here the cases of Ag and Au, for velocities $v=1$ and 10 a.u., and for a distance $z_0=5$ a.u. The solid lines show the values obtained from the optical-data integration, while the dashed lines are

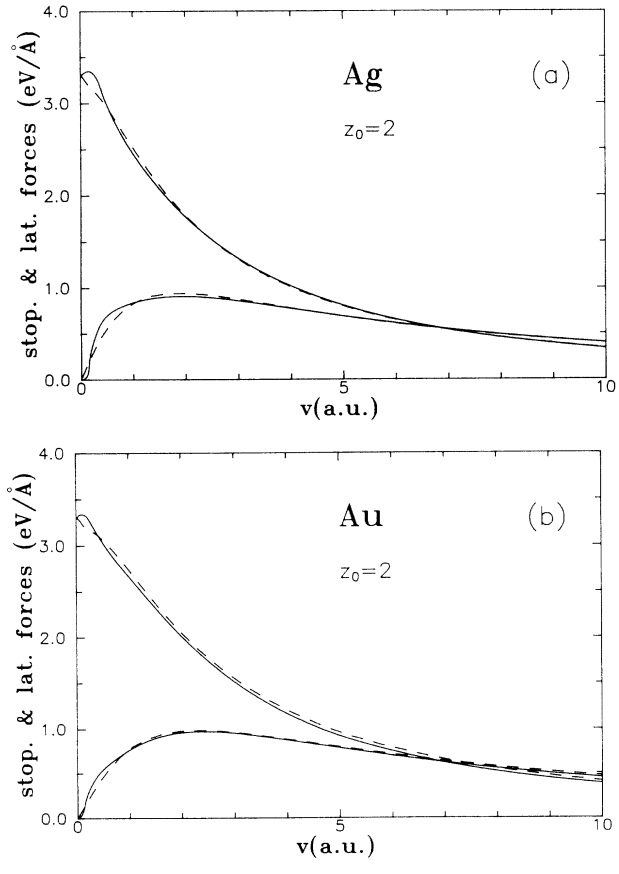

FIG. 8. Comparison between the values of the stopping (lower curves) and lateral (upper curves) forces for (a) Ag and (b) Au. Solid lines: values obtained by numerical integration, from Eqs. (25) and (26), based on the optical data from Ref. [32]; dashed lines: surface-plasma-resonance model, Eqs. (10) and (11), using the ω_s and γ values from Table I.

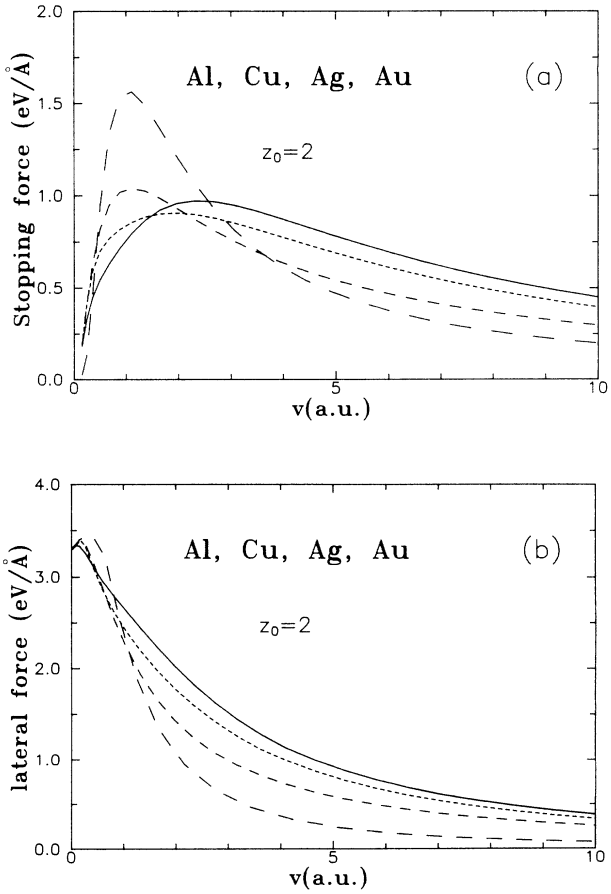

FIG. 9. Comparison between (a) stopping and (b) lateral forces for Al (long-dashed lines), Cu (short-dashed lines), Ag (dotted lines) and Au (solid lines). The force values have been numerically evaluated from Eqs. (25) and (26) using the optical data for each element (Ref. [32]).

those obtained from the surface-plasma-resonance model, with the ω_s and γ values of Table I.

We observe here a new and interesting behavior. While the values for points ahead or very close to the particle ($x=0$) are in very good agreement, significant differences appear as we move to points further in the back of the trajectory. The most revealing discrepancies occur for Ag, where we find a well-defined oscillation with respect to the smooth model prediction. It is interesting to note that even at a relatively low velocity, $v=1$, an oscillatory component appears, superimposed on a more slowly changing function. From the wavelength $\lambda\cong 45$ a.u. of this oscillation and the relation $\lambda=2\pi v/\omega_0$, we readily find that it corresponds to a characteristic frequency $\omega_0\cong 3.8$ eV.

By comparison with Fig. 5, and also with optical data from other sources [37], we find that this value agrees closely with the sharp plasma resonance of Ag at 3.78 eV. Therefore, the modulation in the wake field is associated with the narrow resonance line in the Ag spectrum

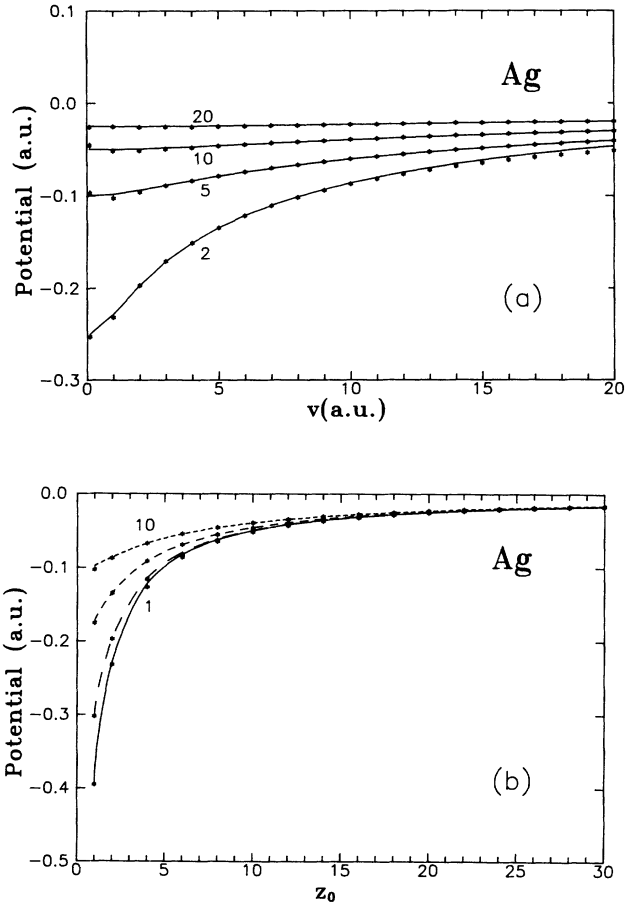

FIG. 10. Comparison between the values of the self-induced dynamical potential for a particle moving at a distance z_0 from an Ag surface. Here the dots are the values obtained by integration of the optical constants, Eq. (24), while the curves are the results of the plasma-resonance model, Eq. (4), using the ω_s and γ values from Table I. (a) illustrates the velocity dependence for $z_0=2$, 5, 10, and 20 a.u., while (b) shows the z_0 dependence for $v=1$ (lower curve), 2, 5, and 10 a.u. (upper curve).

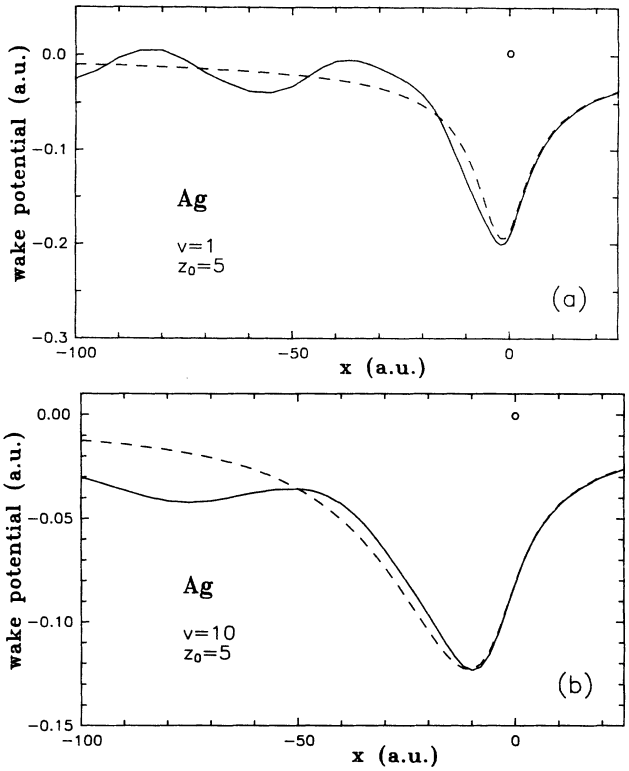

FIG. 11. Wake potential for a particle moving parallel to an Ag surface at a distance $z_0=5$ a.u., and with velocities $v=1$ a.u. (a) and $v=10$ a.u. (b). The values of the wake potential were calculated at $z=0$ (on the surface). Solid lines: values obtained by numerical integration of Eq. (24) using the optical data for Ag (from Ref. [32]). Dashed lines: values calculated from the plasma-resonance model, Eq. (4), using the ω_s and γ values from Table I.

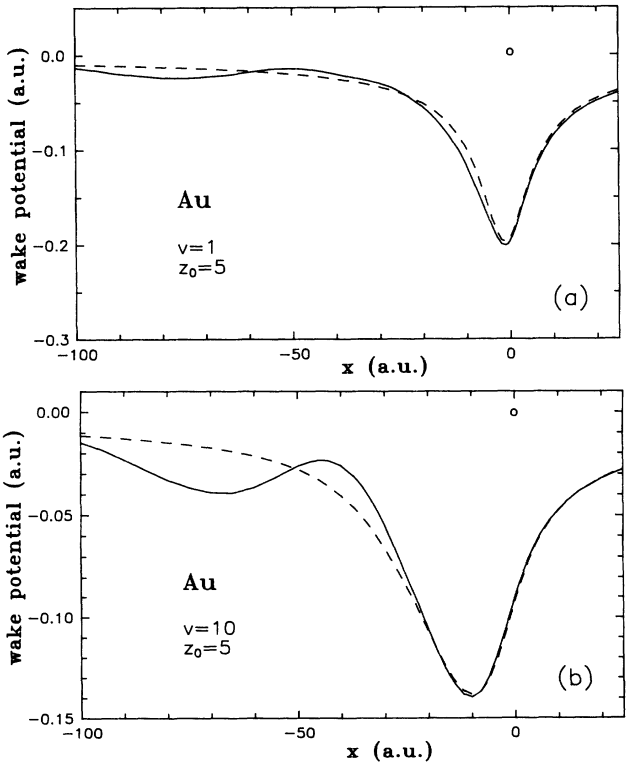

FIG. 12. Same as in Fig. 11, for an Au surface.

shown in Fig. 5.

Thus, contrary to the results obtained from the stopping and lateral forces, and for the potential acting on the moving charge, the results for the potential and fields at larger distances cannot be described by a simple plasma-resonance model (except for nearly-free-electron metals such as Al). A more realistic representation of these quantities can be obtained using the detailed information on the dielectric function over a wide range of frequencies as derived from the optical data for each particular element.

V. DISCUSSIONS AND CONCLUSIONS

Several cases where applications of the present results could be of interest have been listed in Sec. I. It is not the object of the present paper to consider particular applications, but here we can make a few observations that may be of interest for further studies.

One interesting phenomenon recently observed is the acceleration of convoy electrons emitted in ion-surface scattering experiments at grazing angles of incidence [26–31]. The acceleration effect has been explained in terms of the dynamical image field produced by the ion, which would be seen as an acceleration (instead of stopping) field by an electron moving close to the ion [26–29].

In Figs. 9(a) and 9(b), we compared the values of the parallel and perpendicular fields for ions moving parallel to Al, Cu, Ag, and Au surfaces. We notice that at high velocities the force values for these elements appear in the same relative order (i.e., Al-Cu-Ag-Au) as the acceleration effects found in Ref. [30], while a different behavior is expected in the case of low velocities.

Experiments at lower velocities [31] show that the acceleration effect increases with velocity (contrary to the findings for higher velocities). A superposition of the results for low and high velocities [31] appears to indicate the existence of a *maximum* at intermediate velocities, a behavior that is characteristic of the stopping power and in particular is also obtained for the stopping force calculated here. Hence, it would be of considerable interest to get further evidence on these effects by experimentally studying the whole velocity range in a single experiment.

In Fig. 8 we illustrate the values of parallel and perpendicular fields. We observe that these fields have similar behavior at large velocities, while at low velocities the perpendicular forces become stronger. Then, one could expect that in this type of experiment the (repulsive) perpendicular force on the electrons, due to the dominant field induced by the ion, will produce a *deviation of the angular distributions* of the emitted electrons away from the surface; this effect should be more important at lower velocities. This also seems to be at least in qualitative agreement with observations of the angular dependence at high and low velocities in different experiments [27,30,31]. In addition, in Ref. [27] the convoy-electron emission angle has been found to increase with projectile charge. The effect has been qualitatively explained using a simple approximation for the image potential, and hence a quantitative comparison will be desirable.

In summary, the emission of convoy electrons in grazing incidence experiments may become a useful method to explore in more detail the effects of the dynamical image potential and could serve as a test of theoretical models. The main predictions of the model (namely, the maximum in the acceleration effect at intermediate velocities, and the deflection of the angular distributions) seem to be in agreement with experiments, but still more quantitative comparisons would be necessary.

Another problem that we can briefly mention is the energy loss of ion beams specularly reflected at grazing incidence on solid surfaces [12–15]. It has been shown that the experimental results require a good understanding of the contributions due to both long-range collective losses and short-range excitations of single electrons. Obviously, the formulation developed here applies to the collective energy-loss mechanism. Short-range excitations will be important at the closest distances of approach to the surface, and they may be included either by a separate calculation, or as an extension of the present formulation. In the simplest case of nearly-free-electron metals, the RPA model provides a satisfactory solution that includes collective and single-particle excitations [11].

A possible extension of the present description to include short-range processes could be achieved by incorporating spatial-dispersion effects in a dielectric function initially built up from empirical optical data for each element as considered here. An extension of this kind has been introduced earlier by Ritchie and Howie [38], and Ashley [39], to study bulk energy losses in various solids; this approach is currently being considered using an alternative description [40].

We finally summarize the main conclusions of this work.

We have analyzed some of the existing models and analytical expressions frequently used to describe the dynamical image potential and electric field induced by a swift charge moving near a solid surface, in particular for the case of a parallel trajectory.

The characteristics of the induced field in the quasiadiabatic limit have been described in a more general way. The interaction in this limit can be explained in terms of a dynamical component of induced dipole oriented parallel and moving along with the same velocity as the particle. The difference between previous results for the stopping forces corresponding to parallel and perpendicular trajectories can also be explained in terms of the induced dipole moment.

A simple model for the surface response consisting of a broad surface-plasma resonance may provide a satisfactory description of the induced potential and field values *in the proximity* of the moving charge, provided that the model parameters (ω_s and γ) are adequately chosen for each material; this can be achieved by using empirical optical information on a wide range of frequencies. We have determined these values for Al, Cu, Ag, and Au (Table I).

On the other hand, to calculate the values of the induced potential at larger distances from the charge it may be necessary to use the complete optical data for each element. In this way one can describe particular features in the response of real materials or can probe the range of applicability of other models. It seems that this

approach will be useful in investigating, on a more quantitative basis, various processes of atomic interactions near solid surfaces, as in the cases referred to before and others listed in Sec. I.

ACKNOWLEDGMENTS

Stimulating comments from P. M. Echenique, O. Grizzi, and R. Gayet are acknowledged. This work was partially supported by Consejo Nacional de Investigaciones Científicas y Técnicas (PID No. 3-053100, CONICET, Argentina).

APPENDIX: DERIVATION OF EQ. (2)

Let us consider the calculation of the induced potential starting from Eq. (1). It becomes convenient to perform first the integral over the variable q,

$$\int_{-\infty}^{\infty} dq \frac{e^{iqz}}{(\kappa^2+q^2)} \left[\exp(iqz_0) - \exp(-\kappa z_0) \left[\frac{2\epsilon(\omega)}{\epsilon(\omega)+1} \right] \right] = -\frac{\pi}{\kappa} e^{-\kappa(z+z_0)} \left[\frac{\epsilon(\omega)-1}{\epsilon(\omega)+1} \right] , \tag{A1}$$

which can be shown by considering the integration in the complex q plane (note also that both z and z_0 are positive in our case).

Inserting this result in Eq. (1), and separating the $d^2\kappa$ integration in the form

$$\int \frac{d^2\kappa}{\kappa} = \int\int \frac{d\kappa_1 d\kappa_2}{\kappa} = 2\int_{-\infty}^{\infty} d\kappa_1 \int_{\kappa_1}^{\infty} \frac{d\kappa}{\sqrt{\kappa^2-\kappa_1^2}} , \tag{A2}$$

we obtain (with $d\kappa_1 = d\omega/v$)

$$\phi_{\text{ind}}(x,z) = \frac{-Q}{\pi v} \int_{-\infty}^{\infty} d\omega \left[\frac{\epsilon(\omega)-1}{\epsilon(\omega)+1} \right] e^{i\omega x/v} \times \int_{\kappa_1}^{\infty} \frac{d\kappa}{\sqrt{\kappa^2-\kappa_1^2}} e^{-\kappa(z+z_0)} . \tag{A3}$$

The last integral is the Bessel function $K_0(\chi)$, with $\chi = \kappa_1(z+z_0)$.

Finally, if we introduce the integral representation of the K_0 function [34],

$$K_0(\chi) = \int_0^{\infty} \frac{d\xi}{(1+\xi^2)^{1/2}} \cos(\xi\chi) , \tag{A4}$$

we obtain the expression for the induced potential as in Eq. (2).

[1] R. H. Ritchie, Phys. Rev. **106**, 874 (1957); Surf. Sci. **34**, 1 (1973).
[2] R. H. Ritchie and A. L. Marusak, Surf. Sci. **4**, 234 (1966).
[3] J. Harris and R. O. Jones, J. Phys. C **6**, 3585 (1973); **7**, 3751 (1974).
[4] D. Chan and P. Richmond, Surf. Sci. **39**, 437 (1973); J. Phys. C **8**, 2509 (1975); **9**, 163 (1976).
[5] F. Flores and F. García-Moliner, J. Phys. C **12**, 907 (1979).
[6] A. A. Lucas, E. Kartheuser, and R. G. Badro, Phys. Rev. B **2**, 2488 (1970); A. A. Lucas, *ibid.* **20**, 4990 (1979).
[7] G. D. Mahan, Phys. Status Solidi B **55**, 703 (1973).
[8] R. García-Molina, A. Gras-Martí, A. Howie, and R. H. Ritchie, J. Phys. C **18**, 5335 (1985).
[9] T. L. Ferrell, P. M. Echenique, and R. H. Ritchie, Solid State Commun. **32**, 419 (1979).
[10] R. Núñez, P. M. Echenique, and R. H. Ritchie, J. Phys. C **13**, 4229 (1980).
[11] F. J. García de Abajo and P. M. Echenique, Phys. Rev. B **46**, 2663 (1992).
[12] M. Mannami, K. Kimura, K. Nakanishi, and A. Nishimura, Nucl. Instrum. Methods B **13**, 587 (1986).
[13] K. Kimura, M. Hasegawa, and M. Mannami, Phys. Rev. B **36**, 7 (1987); Surf. Sci. **183**, L313 (1987).
[14] K. Kimura and M. Mannami, in *Interaction of Charged Particles with Solid Surfaces,* edited by A. Gras-Martí, H. M. Urbassek, N. R. Arista, and F. Flores (Plenum, New York, 1991).
[15] Y. Fujii, K. Kishine, K. Narumi, K. Kimura, and M. Mannami, Phys. Rev. A **47**, 2047 (1993).
[16] Y. Susuki, T. Ito, K. Kimura, and M. Mannami, J. Phys. Soc. Jpn. **61**, 3535 (1992).
[17] Y. H. Ohtsuki, K. Koyama, and Y. Yamamura, Phys. Rev. B **20**, 5044 (1979).
[18] K. J. Snowdon, D. J. O'Connor, and R. J. MacDonald, Phys. Rev. Lett. **61**, 1760 (1988).
[19] H. Winter, Phys. Rev. A **46**, R13 (1992).
[20] H. J. Andrä, H. Winter, R. Fröhling, N. Kirchner, H. J. Plöhn, W. Wittmann, W. Graser, and C. Varelas, Nucl. Instrum. Methods **170**, 527 (1980).
[21] J. Burgdörfer, Nucl. Instrum. Methods B **24/25**, 139 (1987); **67**, 1 (1992).
[22] P. Focke, S. Suárez, R. Pregliasco, and W. Meckbach, Nucl. Instrum. Methods B **67**, 152 (1992).
[23] L. F. de Ferrariis and R. A. Baragiola, Phys. Rev. A **33**, 4449 (1986).
[24] H. Winter, P. Strohmeier, and J. Burgdörfer, Phys. Rev. A **39**, 3895 (1989).
[25] E. A. Sánchez, M. L. Martiarena, O. Grizzi, and V. H. Ponce, Phys. Rev. A **45**, R1299 (1992).
[26] M. Hasegawa, K. Kimura, and M. Mannami, J. Phys. Soc. Jpn. **57**, 1834 (1988); M. Hasegawa, T. Fukuchi, Y. Mizuno, K. Kimura, and M. Mannami, Nucl. Instrum. Methods B **53**, 285 (1991).
[27] A. Koyama, Y. Sasa, H. Ishikawa, A. Misu, K. Ishii, T. Iitaka, Y. H. Ohtsuki, and M. Uda, Phys. Rev. Lett. **65**, 3156 (1990); A. Koyama, Nucl. Instrum. Methods B **67**, 103 (1992).
[28] T. Iitaka, Y. H. Ohtsuki, A. Koyama, and H. Ishikawa, Phys. Rev. Lett. **65**, 3160 (1990).
[29] K. Kimura, M. Tsuji, and M. Mannami, Phys. Rev. A **46**,

2618 (1992).
[30] H. Ishikawa, A. Misu, A. Koyama, T. Iitaka, M. Uda, and Y. Ohtsuki, Nucl. Instrum. Methods B **67**, 160 (1992).
[31] E. A. Sánchez, O. Grizzi, M. L. Martiarena, and V. H. Ponce, Phys. Rev. Lett. **71**, 801 (1993).
[32] H.-J. Hagemann, W. Gudat, and C. Kunz, J. Opt. Soc. Am. **65**, 742 (1975); cf. also DESY report No. SR-74/7 (1974) (unpublished).
[33] P. M. Echenique, F. Flores, and R. H. Ritchie, Solid State Phys. **43**, 229 (1990).
[34] I. S. Gradshteyn and I. M. Ryzhik, *Tables of Integrals, Series and Products* (Academic, New York, 1965).
[35] N. Takimoto, Phys. Rev. **146**, 366 (1966).
[36] P. M. Echenique and A. Howie, Ultramicrosc. **16**, 269 (1985). The author is grateful to P. M. Echenique for comments on the calculation of the lateral force performed in this reference.
[37] H. Raether, in *Solid State Excitations by Electrons,* edited by G. Höhler, Springer Tracts in Modern Physics Vol. 38 (Springer-Verlag, Berlin, 1965), p. 84; in *Excitation of Plasmons and Interband Transitions by Electrons,* edited by G. Höhler, Springer Tracts in Modern Physics Vol. 88 (Springer-Verlag, Berlin, 1980), p. 1; J. Daniels, C. v. Festenberg, H. Raether, and K. Zeppenfeld, in *Optical Constants of Solids by Electron Spectroscopy,* edited by G. Höhler, Springer Tracts in Modern Physics Vol. 54 (Springer-Verlag, Berlin, 1970), p. 77.
[38] R. H. Ritchie and A. Howie, Philos. Mag. **36**, 463 (1977).
[39] J. C. Ashley, J. Phys. C **3**, 2741 (1991).
[40] I. Abril, R. García-Molina, and N. R. Arista (unpublished).